Direct Ionization Impact on Accelerator Mixed-Field Soft-Error Rate

Rubén García Alía, Maris Tali, Markus Brugger, Matteo Cecchetto, Francesco Cerutti, Andrea Cononetti, Salvatore Danzeca, Luigi Esposito, Pablo Fernández-Martínez, Simone Gilardoni, Angelo Infantino, Maria Kastriotou, Nourdine Kerboub, Giuseppe Lerner, Vanessa Wyrwoll, Véronique Ferlet-Cavrois, César Boatella, Arto Javanainen, Heikki Kettunen, Yolanda Morilla, Pedro Martín-Holgado, Rémi Gaillard, Frédéric Wrobel, Carlo Cazzaniga, Dan Alexandrescu, Maximilien Glorieux, and Helmut Puchner

***Abstract*— We investigate, through measurements and simulations, the possible direct ionization impact on the accelerator soft-error rate (SER), not considered in standard qualification approaches. Results show that, for a broad variety of state-of-the-art commercial components considered in the 65–16-nm technological range, indirect ionization is still expected to dominate the overall SER in the accelerator mixed-field. However, the derived critical charges of the most sensitive parts, corresponding to ∼0.7 fC, are expected to be at the limit of rapid direct ionization dominance and soft-error increase.**

***Index Terms*— Accelerator, CERN, CERN High-energy Accelerator Mixed-field facility (CHARM), FLUKA, large hadron collider (LHC), Monte Carlo method, single-event effects (SEEs), error rate prediction, proton direct ionization**

I. Introduction

LOW-ENERGY singly charged particles are known to be capable of causing single-event upsets (SEUs) in deep sub-micrometer technologies through direct ionization. This has been observed experimentally with low-energy protons [1], muons [2], and electrons [3], for CMOS technology feature sizes of 90 nm and below. Therefore, when using such micro-electronic technologies in environments rich in low-energy singly charged particles, it is important to evaluate their possible impact on the overall soft-error rate (SER) and the related radiation hardness assurance (RHA) implications.

One of the applications and environments for which low-energy protons can potentially have a sizeable impact on the SER is the trapped proton belts for low-earth orbit (LEO) applications as well as a solar flare environment. A detailed RHA study was carried out to evaluate the possible SER impact of low-energy protons [4], not considered in standard proton qualification and SER prediction approaches. The outcome of such a study, based on a broad range of experimental low-energy proton data and space radiation environment conditions, was that, as opposed to requiring a systematic low-energy proton qualification, a safety margin of a factor 5 with respect to the SER derived from the standard qualification (i.e., using the proton SEU cross section in the 20–200-MeV range, as per, e.g., the ESCC 25100 specification) should be applied.

Moreover, low-energy muons, also being capable of inducing soft errors through direct ionization, are considered as a possible prominent contribution to SER in atmospheric applications (e.g., ground level, avionic). For instance, in [5], a detailed simulation study using the MUSCA SEP3 sequential modeling tool [6] showed that muons (as opposed to high-energy neutrons, considered in the JESD89A JEDEC standard) are expected to dominate the atmospheric radiation SER for ground-level applications for CMOS bulk technologies of 28 nm and below. The same work also shows that the fully depleted silicon-on-insulator (FDSOI) and FinFET technologies are expected to be less sensitive to direct ionization from low-energy particles. Alternatively, this article in [7] concludes that terrestrial soft errors induced by the positive and negative muons can be neglected for the SRAMs of the 32-nm planar and 22- and 14-nm trigate technologies.

In the large hadron collider (LHC) high-energy accelerator environment [8], [9], a broad range of particle species are present as produced through the interaction of the TeV energy

Manuscript received July 4, 2019; revised September 26, 2019; accepted October 19, 2019. Date of publication November 4, 2019; date of current version January 29, 2020. This work was supported in part by the European Union's Horizon 2020 Research and Innovation Program under Grant 721624 and in part by the European Space Agency (ESA/ESTEC) at the University of Jyväskylä under Contract 4000124504/18/NL/KML/zk.

R. G. Alía, M. Tali, M. Brugger, M. Cecchetto, F. Cerutti, A. Cononetti, S. Danzeca, L. Esposito, P. Fernández-Martínez, S. Gilardoni, A. Infantino, M. Kastriotou, N. Kerboub, G. Lerner, and V. Wyrwoll are with CERN, CH-1211 Genève, Switzerland (e-mail: ruben.garcia.alia@cern.ch).

V. Ferlet-Cavrois and C. Boatella are with the European Space Agency, ESTEC, 2200 Noordwijk, The Netherlands.

A. Javanainen is with the Department of Physics, University of Jyväskylä, FI-40014 Jyväskylä, Finland, and also with the Electrical Engineering and Computer Science Department, Vanderbilt University, Nashville, TN 37235 USA.

H. Kettunen is with the Department of Physics, University of Jyväskylä, FI-40014 Jyväskylä, Finland.

Y. Morilla and P. Martín-Holgado are with the Centro Nacional de Aceleradores, CSIC, JA, Universidad de Seville, E-41092 Seville, Spain.

R. Gaillard resides in 78730 Saint-Arnoult, France. He is now an Independent Consultant.

F. Wrobel is with the Institut d'Electronique du Sud, Université de Montpellier II/CNRS, 34095 Montpellier, France, and also with the Institut Universitaire de France, 46100 Figeac, France.

C. Cazzaniga is with STFC, Rutherford Appleton Laboratory, Didcot OX11 0QX, U.K.

D. Alexandrescu and M. Glorieux are with IROC Technologies, 38000 Grenoble, France.

H. Puchner is with the Aerospace and Defense Division, Cypress Semiconductor, San Jose, CA 95134 USA.

Color versions of one or more of the figures in this article are available online at http://ieeexplore.ieee.org.

Digital Object Identifier 10.1109/TNS.2019.2951307

This work is licensed under a Creative Commons Attribution 4.0 License. For more information, see http://creativecommons.org/licenses/by/4.0/

protons with different accelerator elements. Such radiation fields are mostly composed of neutrons, protons, pions, photons, and electrons/positrons, and extend from very large energies (GeV range) down to energies compatible with direct ionization sensitivity in deep sub-micrometer technologies. Similar to the space- and ground-level applications, indirect energy deposition (i.e., from protons in space, neutrons in ground-level applications, and protons, neutrons, and pions in accelerators) is assumed to dominate the SER; therefore, the possible contribution from low-energy singly charged particle direct ionization needs to be evaluated. This evaluation is particularly relevant when considering the broad range of digital and mixed signal critical sensing and control accelerator applications [10], [11], requiring the extensive use of commercial off-the-shelf (COTS, e.g., SRAMs, microprocessors, and FPGAs) components exposed to radiation.

An initial evaluation of the possible direct energy deposition impact on the high-energy accelerator SER was presented in [12], based on the simulations and showing that the turning point between the indirect and direct energy deposition soft-error dominances for accelerator applications was expected around 0.3 fC.

II. Low-Energy Charged Particles in the Accelerator Environment

The high-energy accelerator radiation environment is a complex field composed of a broad variety of particles and energies [8], [9], which is typically modeled through advanced Monte Carlo geometries and simulations using the FLUKA tool [13] and monitored by means of the RadMON system [14]. In such an environment, single-event effects (SEEs) in accelerator systems (e.g., magnet powering and protection, beam instrumentation, cryogenics, vacuum, and so on) largely based on COTS components can be highly critical to the performance and availability of the machine [15]. Therefore, components and systems need to be qualified against soft and hard SEEs in order to evaluate the associated error and failure rates, and ensure they are below rates that would compromise the overall availability of the accelerator.

Similar to the high-energy protons in the trapped radiation belt environment and high-energy neutrons at the ground level, SEEs in the accelerator environment are mainly induced by indirect energy deposition (i.e., nuclear reactions) from hadrons in the environment. Therefore, the expected SEE rate is defined as the product of the high-energy hadron (HEH) SEE cross section (typically obtained experimentally with 200-MeV protons) and the HEH equivalent fluence, defined as the fluence of hadrons above 20 MeV plus a weighted neutron contribution in the 0.2–20-MeV range [16]. Hence, this approach does not consider the possible soft-error contribution from the low-energy charged particles.

In addition to the SEE characterization, using 200-MeV protons, components, boards, and systems can be tested in the CERN High-energy Accelerator Mixed-field facility (CHARM) [17], where the high-energy accelerator environment is reproduced at an accelerated rate by means of protons interacting with a 50-cm copper target. Different test positions and configurations are available

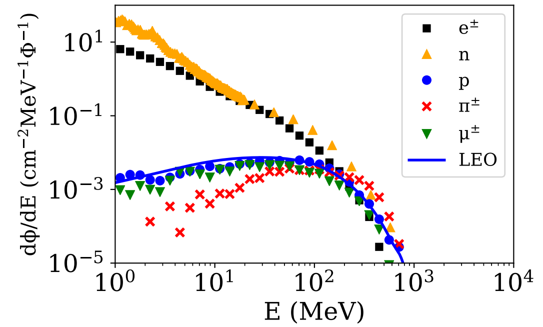

Fig. 1. Particle energy spectra of singly charged particles in the LEO orbit (proton spectrum for 800 km, 98°, 100-mil aluminum shielding) and the G0 position at CHARM, normalized to the respective integrated proton flux above 20 MeV for each of the two environments. For the G0 position at the CHARM, neutrons are also included.

depending on the application radiation levels, composition, and energy spectra. Experimental results shown in this article correspond to a facility operation with the movable shielding outside of the irradiation hall and with the device under test located in the so-called G0 position, roughly 7 m from the target at a 90° angle with respect to the primary proton beam.

The singly charged particle energy spectra for such position and configuration are plotted in Fig. 1 as simulated in FLUKA and normalized to the integrated proton flux above 20 MeV. The plot also includes the normalized LEO proton spectrum for an 800-km, 98° orbit considering a 100-mils aluminum shielding, as retrieved from CREME96 [18]. As can be seen, the CHARM- and LEO-normalized proton spectra are highly comparable in the full-energy range considered (1–1000 MeV). In addition to protons, lighter charged particles, such as positive and negative muons and pions, are also present in the mixed field, in similar proportions as protons and with comparable energy distributions. Finally, electrons and positrons are present, in alike proportions as protons above 100 MeV (and, therefore, extending to much larger energies than the trapped-belt electrons around earth) and with significantly larger fluxes below that energy. Neutrons, while being charge-neutral, are also included for completeness.

It is to be noted that this specific mixed-field environment is not necessarily the representative of other possible accelerator-like environments with, e.g., a different proportion of low-energy singly charged particles and HEHs. Therefore, in order to consider the radiation environments in the actual LHC accelerator, we investigate the particle energy spectra of two regions near the interaction point 1 (IP1) of the LHC. The source of radiation in this area is the collision debris at 14-TeV center-of-mass energy, considering an 85-mb proton–proton collision cross section. Results are normalized to 100 fb^{-1}, corresponding to roughly three months of operation for high-luminosity LHC (HL-LHC) conditions. An inverse femtobarn (fb^{-1}) is the unit of integrated luminosity and corresponds to roughly 10^{14} proton–proton inelastic collisions at TeV energies. The choice of the integrated luminosity as the normalization parameter is linked to the fact that, near the IPs in a high-energy accelerator, the radiation levels scale with the number of collisions.

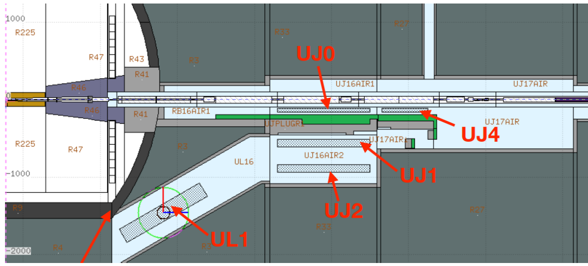

Fig. 2. Top view of the FLUKA geometry for the accelerator regions near IP1. The areas of interest for the results presented in this article are UJ0, as a representative of the tunnel, and UJ1, as a representative of the shielded areas.

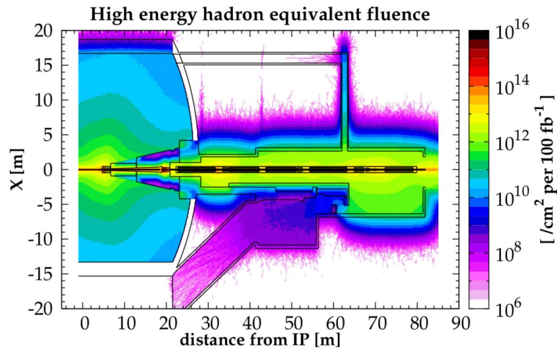

Fig. 3. Top view of the simulated HEH equivalent fluence values for the geometry introduced in Fig. 2 and corresponding to an integrated luminosity of 100 fb^{-1}.

Moreover, simulations were performed with the HLLHCV1.0 optics and the 590-μrad vertical crossing angle. Particle production and transport thresholds were set to 1 MeV (except for neutrons, for which the threshold was set to 0.01 meV) and the electromagnetic part of the showers was disabled in order to enhance the CPU performance of the runs. A more complete description of the expected radiation levels near the HL-LHC high-luminosity IPs can be found in [9].

A top view of the simulated geometry can be seen in Fig. 2, where the IP is to the left and the LHC tunnel geometry extends 80 m away from the IP. The two regions selected for analysis in this article are UJ0 (in the tunnel) and UJ1 (in the shielded alcove area). A 2-D top view of the simulated radiation levels can be seen in terms of HEH equivalent fluences per 100 fb^{-1}, as shown in Fig. 3. The radiation levels for the UJ0 and UJ1 locations are summarized in Table I, in this case normalized to 250 fb^{-1}, which corresponds to the nominal annual integrated luminosity for the HL-LHC operation. Note that the LHC typically operates during seven months per year (from May to November, both included).

As a reference, levels in UJ1 are the representative of the shielded alcoves near the IPs, hosting a very large quantity of critical systems based on commercial electronic components. Therefore, special care needs to be devoted in their design and radiation qualification in order to ensure the necessary tolerance for a satisfactory performance and availability of the accelerator. Whereas cumulative radiation damage in these shielded areas is certainly a concern (e.g., for a 12-year HL-LHC lifetime, integral values would correspond to roughly 40 Gy and 4 × 10^{11} MeV n_{eq}/cm^2), the main threat is SEEs, mainly due to the large number of active semiconductor components and system units present.

As to what regards the tunnel area near the IP (UJ0) levels are clearly too large to host commercial active electronic components. However, the particle energy spectra in these locations can be considered as representative of other LHC tunnel areas with lower absolute radiation levels and where commercial electronics is installed.

The normalized particle energy spectra for the two locations considered are shown in Figs. 4 and 5, for the tunnel and the shielded area, respectively. Despite the very different absolute radiation levels (see Table I), the spectra bear similarities among each other and with that at CHARM (see Fig. 1). However, it is already visible that, as expected and when compared with the neutron flux, charged particles are less prominent in the shielded areas. The impact of the different particle

TABLE I

EXPECTED ANNUAL RADIATION LEVELS IN THE UJ0 (TUNNEL) AND UJ1 (SHIELDED AREA) LOCATIONS SHOWN IN FIG. 2. VALUES ARE NORMALIZED TO 250 fb^{-1}, CORRESPONDING TO THE NOMINAL ANNUAL HL-LHC INTEGRATED INTENSITY. A MORE COMPLETE DESCRIPTION OF THE EXPECTED RADIATION LEVELS NEAR THE HL-LHC HIGH-LUMINOSITY IPS CAN BE FOUND IN [9]

Region	HEH$_{eq}$ (cm^{-2})	1MeV$_{neq}$ (cm^{-2})	TID
UJ0 (tunnel)	4.3×10^{12}	4.5×10^{13}	1.9 kGy
UJ1 (shielded)	1.7×10^{9}	3.3×10^{10}	3.5 Gy

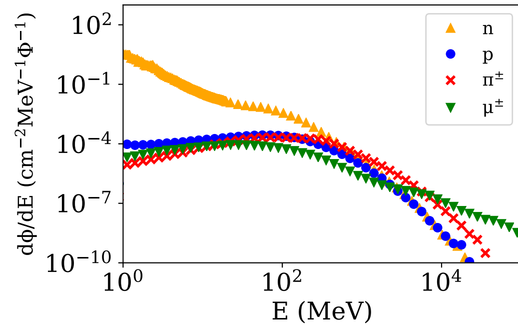

Fig. 4. Particle energy spectra at the UJ0 tunnel location, normalized to the HEH fluence.

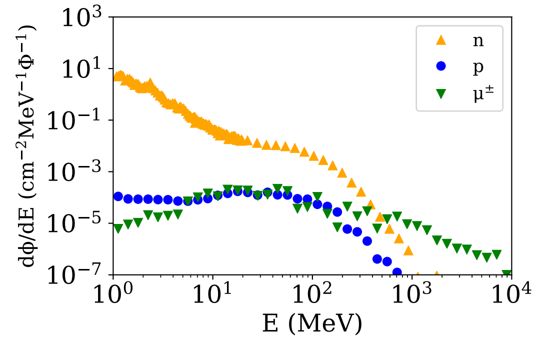

Fig. 5. Particle energy spectra at the UJ1 shielded location, normalized to the HEH fluence. Charged pions are not included due to their negligible fluxes.

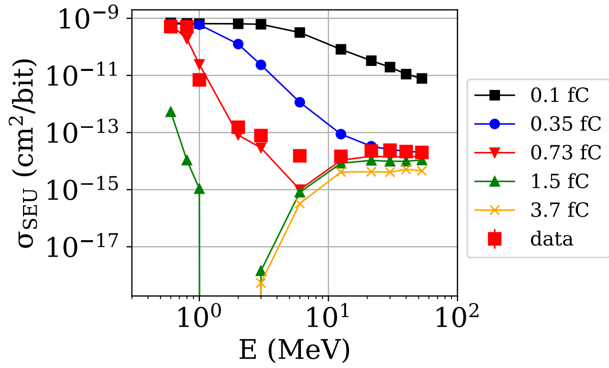

Fig. 6. Proton cross section for the ISSI 65-nm part as measured experimentally at RADEF, and including the simulated values using a 250-nm RPP model with different critical charges.

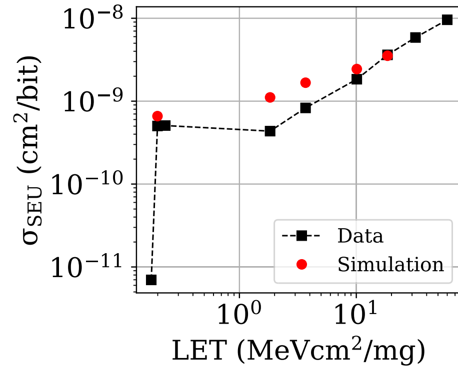

Fig. 7. Heavy-ion SEU cross section for the ISSI 65-nm part as measured experimentally at RADEF and including the simulated values using the nested RPP model described in the text. The experimental points, from lower to larger LET, correspond to 1-MeV, 800-keV, and 600-keV protons and 9.3-MeV/n N, Ne, Ar, Fe, Kr, and Xe ions, and are all at normal beam incidence.

energy spectra described in this section on the expected SER will be evaluated and discussed in Section IV.

III. Low-Energy Proton SEU Cross Section: Measurement and Simulations

A. RPP Model for 65-nm ISSI SRAM

An important fraction of the experimental work presented in this article was performed in the scope of a doctoral thesis among ESA, the University of Jyvaskyla, and CERN [19]. A 65-nm bulk CMOS SRAM memory (reference IS61WV204816BLL by ISSI) suspected to be highly sensitive to low-energy protons was selected to perform the study presented in this article. Proton tests were performed in the RADEF facility on unpackaged devices, using two different beam lines: the low-energy line in vacuum up to 5 MeV and the high-energy line in air above that value and up to 53 MeV. In the low-energy line, the mono-energetic beams of 600 keV, 800 keV, and 1, 2, and 3 MeV were used. Such energies are obtained by degrading a 6-MeV primary proton beam from the JYFL K-130 cyclotron and selecting the energy of interest through a magnetic field, providing a full-width half-maximum energy value of roughly 25 keV in the full 500-keV to 5-MeV energy range [20].

The retrieved experimental proton SEU cross section is shown in Fig. 6, exhibiting a prominent peak in the 600–800-keV range, with a cross section of a factor $\sim 2 \times 10^4$ larger than the high-energy saturation value. In addition, the FLUKA Monte Carlo code was used to simulate the SEU cross section for a cubic rectangular parallelepiped (RPP) model of 250-nm side and 6-μm SiO_2 back-end-of-line (BEOL). The FLUKA version used was FLUKA2011 2x.6 from March 2019. Charged particle production and transport energies were set to the minimum value of 1 keV, corresponding to 0.044 fC or 275 electrons, in order to accurately account for energy-deposition events in submicrometer volumes.

The resulting simulated SEU cross sections are shown in Fig. 6 for different critical charges. As can be seen, the agreement of the experimental data with the 0.73-fC simulated curve, with the exception of the 6-MeV point (potentially dominated by elastic Coulomb scattering), is highly satisfactory. Indeed, the retrieved best fit critical charge is also very compatible with the expectations from the SPICE models for this same technology [21]. It is also worth highlighting that as the critical charge value is increased, the classical indirect energy deposition curves (e.g., for 3.7 fC) are retrieved, falling off at a few MeV owing to the proton Coulomb barrier with silicon. The latter can be typically fit to a Bendel, Weibull, or Lognormal function [22], which is clearly not the case for SEU cross sections impacted by direct ionization.

Likewise, when Q_{crit} is reduced, the low-energy proton peak is broadened (e.g., for 0.35 fC), until eventually also high-energy, minimum ionizing protons become capable of inducing SEUs through direct ionization (e.g., $Q_{\text{crit}} \sim 0.1$ fC), therefore also impacting the high-energy saturation value.

B. Extension to Heavy Ions and Nested RPP Model

One of the limitations of the RPP model is that regions in the simulation are categorized as either outside the sensitive volume (SV) (no charge collection) or inside it (100% charge collection). In reality, whereas the p-n junction area of the SRAM off transistors can be approximated to a 100% charge collection efficiency (CCE) area where the generated charges are collected by drift in the electric field region, charge collection can also occur by diffusion. Therefore, instead of a single RPP region with a factor 1 CCE, a nested RPP model, as proposed in [1] and [23], can be defined in order to consider diffusion. The latter is defined through different nested volumes with the associated CCE factors, calibrated to the heavy-ion data.

Provided that, in addition to low energy proton data, heavy ion data were also collected for the ISSI 65-nm part in the scope of this article, both data sets are shown in Fig. 7 as a function of linear energy transfer (LET). However, it is to be noted that the notion of the LET for low-energy protons bears a more indirect link to the deposited energy than that in the case of ions, mainly owing to the very limited low-energy proton range, large energy-deposition straggling, and significant variability of the LET as a function of depth.

Whereas the single RPP model would result in a simulated heavy-ion SEU cross section with the shape of a step-function equal to zero below the LET threshold and to the sensitive

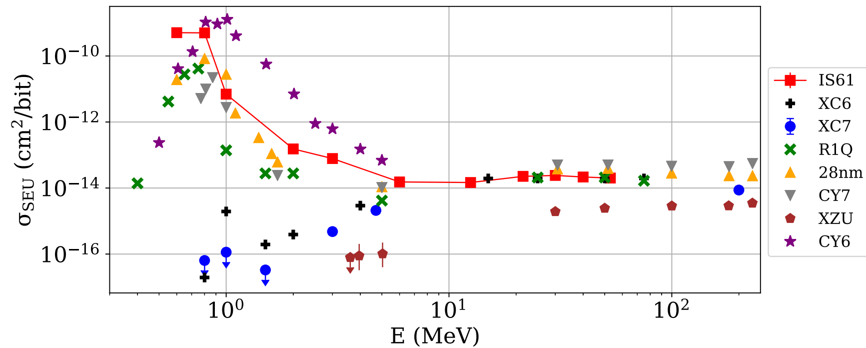

Fig. 8. Experimental proton cross sections for different deep sub-micrometer bulk CMOS parts. The full references, technologies, and (where applicable) literature citations can be found in Table II.

TABLE II

COMPONENTS FOR WHICH LOW-ENERGY PROTON DATA ARE PLOTTED IN FIG. 8. FOR THE TWO FIRST, DATA WERE RETRIEVED IN THE SCOPE OF THIS ARTICLE. THE NEXT THREE ARE FROM THE ESA/IROC TECHNOLOGIES PROJECT, AND THE FINAL THREE ARE FROM THE LITERATURE

Part Reference	Short Name	Function	Tech.
IS61WV204816BLL	IS61	Async. SRAM	65 nm
CY62167GE30-4 5ZXI	CY6	Async. SRAM	65 nm
Anonymous 28 nm SRAM	28 nm	Async. SRAM	28 nm
CY7C2562XV18	CY7	QDR SRAM	65 nm
XZU3EG	XZU	FPGA	16 nm finFET
XC6SLX9-2TQG144I [27]	XS6	FPGA	45nm
XC7A35T-1CPG236C [28], [29]	XC7	FPGA	28 nm
R1QBA7218ABG-22IB0 [27]	R1Q	DDR SRAM	45nm

surface above it, the nested RPP approach allows for a more realistic representation of the experimental data, as shown in Fig. 7. In this case, the CREME MC online simulation tool [24], [25] was used, allowing defining the different nested SVs and CCEs directly. As defined, the model is not capable of accurately describing the experimental SEU cross section for the intermediate LET values ($1.8 - 3.7$ MeVcm^2/mg), where it overestimates the data by a factor $\sim$2. For higher and lower LET values (the latter being relevant for direct ionization from protons), the agreement is highly satisfactory. In any case, the nested RPP model defined in this way allows for the comparison between it and the single RPP in terms of indirect energy deposition. When running both models with 53-MeV protons (for which, at a critical charge of 0.73 fC, inelastic energy-deposition dominates), the difference in the resulting SEU cross section was retrieved as 1% and, therefore, compatible with the statistical uncertainty of the simulation. It is to be highlighted that the single and nested RPP models have the same central volume of 250-nm side as well as the same critical charge. Therefore, adding larger volumes with lower CCEs, whereas allowing to reproduce the heavy-ion data more accurately, has a negligible impact on the energy deposited by high-energy protons through indirect ionization.

Thus, we conclude that the single RPP model used in this article is capable of successfully reproducing both the low-energy proton direct ionization as well as the high-energy proton indirect ionization experimental behavior. This is an important result as it means that, despite not being capable of providing a physical response for heavy ions, the model is accurate enough to evaluate the impact of low-energy singly charged particles and HEHs, both of interest in the high-energy accelerator mixed-field environment.

C. Extension to Other Low-Energy Proton SEU Data

In addition to the 65-nm ISSI reference studied in this article, a collection of low-energy proton data from commercial deep-submicrometer bulk technologies available in the literature as well as first published in this article is presented in Fig. 8. The full references, functions, and technologies (i.e., node sizes) are shown in Table II. The parts short named 28 nm, CY7, and XZU were tested in the framework of an ESA/IROC Technologies project. Low-energy proton tests for these parts were performed at RADEF. The XZU device is flip-chip; hence, irradiation was performed from the backside, with the lid removed and the substrate thinned to 120 μm. The SEU results for this part correspond to the block RAM (BRAM).

The plot also includes recent low-energy proton results from the 65-nm Cypress SRAM (CY62167GE30-4 5ZX1, here short named CY6) using the tandem accelerator at the "Centro Nacional de Aceleradores" in Seville, Spain [26]. This memory is equipped with ECC, which was disabled during the tests. As can be seen, its sensitivity is even larger than the IS61 one.

Therefore and with the exception of CY6, the reference studied in this article can be considered as a worst case low-energy proton sensitivity, with three components (R1Q, CY7, and 28 nm) having a response similar to it, another (XC6) showing a very weak sensitivity to low-energy protons, and, finally, XC7 and XZU not being at all sensitive below a few MeV.

IV. MIXED-FIELD ENERGY-DEPOSITION DISTRIBUTION AND SEU CROSS SECTION

The same reference that was tested for low-energy protons (IS61) was irradiated in the CHARM mixed-field facility at CERN. As described in Section II, the experimental location

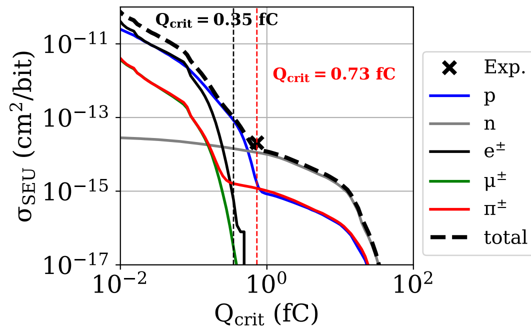

Fig. 9. Simulated SEU cross section for the CHARM G0 location as a function of critical charge for the 250-nm RPP model, showing the different particle contributions. The experimental SEU cross-sectional value for IS61 is also plotted for the considered critical charge value of 0.73 fC, showing very good agreement between simulation and experiment.

and configuration used were G0, with copper target and no shielding. The SRAM memory was accessed during irradiation through a commercial radiation-tolerant flash-based FPGA and was covered with a 4-mm boron carbide layer to exclude potential soft-error contribution from thermal neutrons. Under these conditions, the retrieved experimental HEH SEU cross section was 2.06×10^{-14} cm^2/bit.

In order to estimate the contribution of the different particle species to the mixed-field SER, Monte Carlo simulations were performed using FLUKA. The CHARM radiation environment introduced in Section II is used together with the RPP model presented in Section III to retrieve the energy-deposition distribution from the various mixed-field particles. Such distributions are divided by the HEH fluence, considered as the standard SEE figure of merit, and can, therefore, be interpreted as HEH cross sections.

The resulting SEU cross-sectional contributions from the different particles can be seen in Fig. 9. As can be observed, the indirect energy-deposition part of the curve ($Q_{crit} > 1$ fC) is clearly dominated by neutrons, with protons and pions, also capable of depositing energy through nuclear interactions, each having a factor ~10 lower contributions. Moreover, the part of the curve for which direct ionization starts to dominate ($Q_{crit} < 0.7$ fC) has a prevailing proton contribution to the SEU cross section. Charged muons and pions, despite having a similar energy spectrum as protons, as shown in Fig. 1, have a lower contribution owing to their reduced mass and LET. Likewise, electrons, despite having a much larger low-energy flux, only start having a comparable contribution with protons below 0.1 fC. Therefore, despite the broad variety of low-energy singly charged particles present in the mixed-field environment, at least for this specific study case, the direct ionization is dominated by low-energy protons and can be considered as very similar to that in the trapped proton belt in space.

It is also noteworthy that the experimental cross-sectional value for the ISSI 65-nm part in CHARM, when plotted as a function of the assumed critical charge value of 0.73 fC, is highly compatible with the simulated value, still expected to be dominated by indirect ionization. However, it is also important to highlight that, according to the considered model, the device sensitivity is at the limit of entering the part of the curve dominated by direct ionization and is therefore expected to, as opposed to the indirect energy deposition interval, have a very strong SEU cross section dependence with critical charge.

V. RHA Implications

The experimental results presented in this article for a commercial 65-nm bulk CMOS SRAM show that, despite the very strong sensitivity to low-energy protons of over four orders of magnitude larger than the high-energy saturation value, the impact of direct ionization from singly charged low-energy particles (protons, muons, pions, electrons, and positrons) in the mixed-field accelerator environment is negligible with respect to the dominating indirect ionization. Therefore, the standard qualification approach of deriving the soft-error sensitivity using high-energy cyclotron proton testing to extract the respective SEU cross-sectional value and obtaining the SER by multiplying it with the HEH fluence in operation is still valid.

Such conclusion applies to the 65-nm bulk CMOS SRAM considered in this article as well as by extension to other state-of-the-art commercial parts with similar or lower SEU cross sections, as shown in Section III. The outcome of this article is also supported by a 250-nm RPP model representative of the technology considered. However, the simulated results also indicate that a critical charge value of ~0.7 fC, as determined for the studied reference, marks the limit between the indirect and direct ionization soft-error dominances for the accelerator environment. Therefore, for more sensitive parts, the standard high-energy accelerator qualification approach could result in a significant underestimation of the operational SER.

For instance, if a critical charge of 0.35 fC is considered, as shown in Fig. 6, the expected high-energy proton saturation cross section would be $\sim 2 \times 10^{-14}$ cm^2/bit, whereas, as can be seen in Fig. 9, the mixed-field SER would correspond to an HEH cross section of 10^{-13} cm^2/bit, i.e., five times larger than that retrieved from the HEH approach. For even lower critical charges however, such as 0.1 fC, the high-energy proton cross section would already exhibit a significant increase with respect to larger critical charges owing to the impact of direct ionization also at these minimum ionizing energies. In this situation, the high-energy proton cross section would again be an appropriate figure of merit to derive the mixed-field SER, however in this case not multiplied by the HEH flux (which is linked to indirect ionization) but rather by the high-energy singly charged particle flux.

The discussion above can be better interpreted when looking at Fig. 10, showing the energy-deposition curves for the three mixed-field environments considered (CHARM, LHC tunnel, and LHC-shielded), plus for 53-MeV protons, regarded as the representative of standard SEU testing for space and accelerator applications (indeed, for destructive SEEs, larger energies of up to 200 MeV or beyond are required, but for soft errors, 50 MeV is typically enough to be in the SEU cross-sectional saturation region). As a first important observation, the energy-deposition distribution in the direct ionization regions are very similar for the CHARM and LHC tunnel areas and lower in the case of the LHC-shielded area, owing to the reduced relative

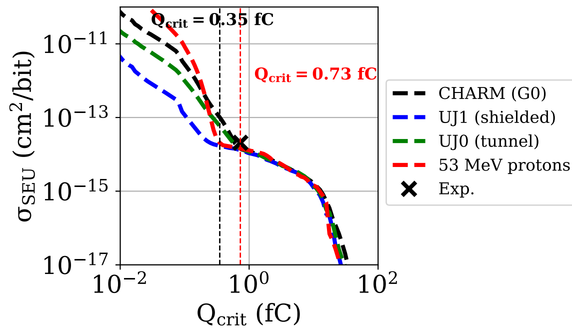

Fig. 10. Simulated SEU cross section as a function of critical charge for the CHARM G0 location (as shown in Fig. 9, including the different individual mixed-field contributions) and the tunnel and shielded accelerator locations introduced in Section II. The 53-MeV mono-energetic proton curve is also included for comparison.

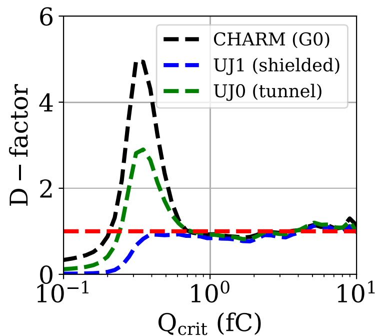

Fig. 11. Ratio between the expected operational SER and that retrieved from the high-energy proton used standard qualification. As the excess is linked to direct ionization, the value is defined as the *D*-factor. In both cases, results are obtained using the 250-nm RPP model described in the text.

charged particle presence in the environment. Second, it is worth noting that 53-MeV protons are representative of the mixed-field energy deposition in a very broad critical charge range and that there is only a small window in which the mixed-field values are significantly larger.

In order to further quantify the direct ionization impact, Fig. 11 shows the simulated ratio between the mixed field SER and that expected from high-energy protons, defined as *D*-factor (for direct ionization). In other words, such a value corresponds to the underestimation of the application SER due to direct ionization when using high-energy proton experimental data to retrieve it. As can be seen, down to ~0.7 fC, the ratio is 1, showing that the standard high-energy proton qualification is, as expected, the representative of indirect energy deposition in the mixed field. Below this value however, direct ionization dominates, inducing an underestimation up to a factor 5, which then progressively decreases as high-energy protons start to also induce soft errors via direct ionization.

With the purpose of generalizing the result, the same simulation approach as that yielding the results shown in Fig. 11 is applied to different cubic-SV sizes in order to evaluate the impact of the latter on the respective *D*-factor. In this case, in the x-axis, the LET (in units of fC/μm) is used

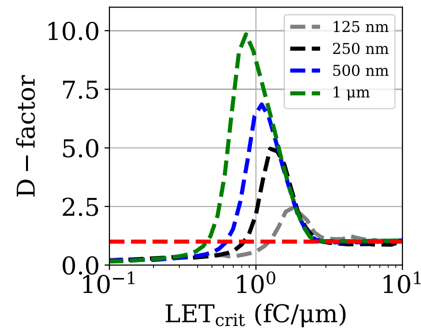

Fig. 12. *D*-factor values for the CHARM G0 environment for different cubic Sensitive Volume side sizes. The black, 250-nm curve corresponds to the same one for CHARM (G0) in Fig. 11.

as opposed to the critical charge in order to allow for a more direct comparison between different SV thickness cases. It can be useful to note that 1 fC/μm corresponds to roughly 0.1 MeVcm^2/mg in silicon in the standard LET units.

As can be seen in Fig. 12, as the SV increases, larger *D*-factors are obtained, which can be attributed in first approximation to the larger number of stopping singly charged particles in the SV.

VI. Conclusion

The importance of evaluating the possible soft-error impact of direct ionization in a mixed-field accelerator environment is motivated first of all by the presence of a broad variety of singly charged particles capable of depositing energy through direct ionization, and secondly the fact that the latter are not considered in the standard high-energy proton qualification approach. Experimental and simulation results shown in this article suggest that for presently available COTS parts built on bulk and FinFET CMOS technologies in the 16–65-nm range, the SER in mixed-field accelerator applications is not expected to be affected by direct ionization. Even if lower critical charges are considered, a safety margin of a factor 5 with respect to the traditional qualification would be sufficient to account for possible low-energy direct ionization effects in the accelerator mixed-field environment. This conclusion is compatible with that derived in [4] for space applications, which is also consistent with the similarity between the LEO and the mixed-field proton spectra (including the low-energy range) and the mixed-field dominance of proton direct ionization with respect to other charged particles such as electrons, positrons, and positive and negative muons and pions. Moreover, the factor 5 is found to be even more conservative when considering technologies with smaller sensitive volumes, which is a relevant result for scaling trends.

Nevertheless, the fact that relatively high-energy protons (~50 MeV) available in standard cyclotron SEE facilities are representative, within a factor 5 of the direct ionization impact on mixed-field environments should not mask the fact that, in absolute terms and considering a constant SV, SERs would increase by three orders of magnitude when moving from 1- to 0.1-fC critical charge values.

It is also relevant to conclude that in the accelerator mixed-field and despite the broad range of singly charged particles in the environments, protons dominate the direct ionization energy deposition and exhibit a spectral shape very similar to that of a shielded LEO environment. Moreover, this article also shows that a simple RPP model is sufficient for describing the proton low-energy direct ionization and high-energy indirect ionization for a 65-nm technology, yielding compatible results as those obtained with a more realistic nested RPP model also capable of reproducing the heavy-ion response.

REFERENCES

[1] B. D. Sierawski *et al.*, "Impact of low-energy proton induced upsets on test methods and rate predictions," *IEEE Trans. Nucl. Sci.*, vol. 56, no. 6, pp. 3085–3092, Dec. 2009.

[2] B. D. Sierawski *et al.*, "Muon-induced single event upsets in deep-submicron technology," *IEEE Trans. Plasma Sci.*, vol. 57, no. 6, pp. 3273–3278, Dec. 2010.

[3] M. P. King *et al.*, "Electron-induced single-event upsets in static random access memory," *IEEE Trans. Nucl. Sci.*, vol. 60, no. 6, pp. 4122–4129, Dec. 2013.

[4] N. A. Dodds *et al.*, "The contribution of low-energy protons to the total on-orbit SEU rate," *IEEE Trans. Nucl. Sci.*, vol. 62, no. 6, pp. 2440–2451, Dec. 2015.

[5] G. Hubert, L. Artola, and D. Regis, "Impact of scaling on the soft error sensitivity of bulk, FDSOI and FinFET technologies due to atmospheric radiation," *Integr., VLSI J.*, vol. 50, pp. 39–47, Jun. 2015.

[6] G. Hubert, S. Duzellier, C. Inguimbert, C. Boatella-Polo, F. Bezerra, R. and Ecoffet, "Operational SER calculations on the SAC-C orbit using the multi-scales single event phenomena predictive platform (MUSCA SEP^3)," *IEEE Trans. Nucl. Sci.*, vol. 56, no. 6, pp. 3032–3042, Dec. 2009.

[7] N. Seifert, S. Jahinuzzaman, J. Velamala, and N. Patel, "Susceptibility of planar and 3D tri-gate technologies to muon-induced single event upsets," in *Proc. Int. Rel. Phys. Symp.*, Apr. 2015, pp. 2C.1.1–2C.1.6.

[8] K. Roeed *et al.*, "Method for measuring mixed field radiation levels relevant for SEEs at the LHC," *IEEE Trans. Nucl. Sci.*, vol. 59, no. 4, pp. 1040–1047, Aug. 2012.

[9] R. G. Alía *et al.*, "LHC and HL-LHC: Present and future radiation environment in the high-luminosity collision points and RHA implications," *IEEE Trans. Nucl. Sci.*, vol. 65, no. 1, pp. 448–456, Jan. 2018.

[10] S. Uznanski, B. Todd, A. Dinius, Q. King, and M. Brugger, "Radiation hardness assurance methodology of radiation tolerant power converter controls for Large Hadron Collider," *IEEE Trans. Nucl. Sci.*, vol. 61, no. 6, pp. 3694–3700, Dec. 2014.

[11] R. Denz, E. de Matteis, A. Siemko, and J. Steckert, "Next generation of quench detection systems for the high-luminosity upgrade of the LHC," *IEEE Trans. Appl. Supercond.*, vol. 27, no. 4, Jun. 2017, Art. no. 4700204.

[12] A. Infantino, R. G. Alía, and M. Brugger, "Monte Carlo evaluation of single event effects in a deep-submicron bulk technology: Comparison between atmospheric and accelerator environment," *IEEE Trans. Nucl. Sci.*, vol. 64, no. 1, pp. 596–604, Jan. 2017.

[13] T. T. Böhlen *et al.*, "The FLUKA code: Developments and challenges for high energy and medical applications," *Nucl. Data Sheets*, vol. 120, pp. 211–214, Jun. 2014.

[14] G. Spiezia *et al.*, "A new RadMon version for the LHC and its injection lines," *IEEE Trans. Nucl. Sci.*, vol. 61, no. 6, pp. 3424–3431, Dec. 2014.

[15] R. G. Alía *et al.*, "Single event effects in high-energy accelerators," *Semicond. Sci. Technol.*, vol. 32, no. 3, Feb. 2017, Art. no. 034003. [Online]. Available: http://stacks.iop.org/0268-1242/32/i=3/a=034003

[16] M. Cecchetto, R. G. Alía, S. Gerardin, M. Brugger, A. Infantino, and S. Danzeca, "Impact of thermal and intermediate energy neutrons on SRAM SEE rates in the LHC accelerator," *IEEE Trans. Nucl. Sci.*, vol. 65, no. 8, pp. 1800–1806, Aug. 2018.

[17] J. Mekki, M. Brugger, R. G. Alia, A. Thornton, N. C. Dos Santos Mota, and S. Danzeca, "CHARM: A mixed field facility at CERN for radiation tests in ground, atmospheric, space and accelerator representative environments," *IEEE Trans. Nucl. Sci.*, vol. 63, no. 4, pp. 2106–2114, Aug. 2016.

[18] A. J. Tylka *et al.*, "CREME96: A revision of the cosmic ray effects on micro-electronics code," *IEEE Trans. Nucl. Sci.*, vol. 44, no. 6, pp. 2150–2160, Dec. 1997.

[19] M. Tali, "Single-event radiation effects in hardened and state-of-the-art components for space and high-energy accelerator applications," Ph.D. dissertation, Dept. Phys., Univ. Jyväskylä, Jyväskylä, Finland, 2019. [Online]. Available: https://jyx.jyu.fi/handle/123456789/64284

[20] H. Kettunen *et al.*, "Low energy protons at RADEF—Application to advanced eSRAMs," in *Proc. IEEE Radiat. Effects Data Workshop (REDW)*, Jul. 2014, pp. 1–4.

[21] F. Wrobel, A. D. Touboul, L. Dilillo, and F. Saigné, "Soft error triggering criterion based on simplified electrical model of the SRAM cell," *IEEE Trans. Nucl. Sci.*, vol. 60, no. 4, pp. 2537–2541, Aug. 2013.

[22] E. L. Petersen, "The SEU figure of merit and proton upset rate calculations," *IEEE Trans. Nucl. Sci.*, vol. 45, no. 6, pp. 2550–2562, Dec. 1998.

[23] K. M. Warren *et al.*, "The contribution of nuclear reactions to heavy ion single event upset cross-section measurements in a high-density SEU hardened SRAM," *IEEE Trans. Nucl. Sci.*, vol. 52, no. 6, pp. 2125–2131, Dec. 2005.

[24] *CREME site by the Vanderbilt University School of Engineering*. [Online]. Available: https://creme.isde.vanderbilt.edu/

[25] M. H. Mendenhall and R. A. Weller, "A probability-conserving cross-section biasing mechanism for variance reduction in Monte Carlo particle transport calculations," *Nucl. Instrum. Methods Phys. Res. A, Accel., Spectrometers, Detectors Associated Equip.*, vol. 667, pp. 38–43, Mar. 2012.

[26] Y. Morilla *et al.*, "Progress of CNA to become the Spanish facility for combined irradiation testing in aerospace," in *Proc. Eur. Conf. Radiat. Effects Compon. Syst. (RADECS)*, Sep. 2018.

[27] N. Sukhaseum *et al.*, "Risk assessment of electron induced SEE during the JUICE mission," 2018.

[28] G. Tsiligiannis *et al.*, "Radiation effects on deep submicrometer SRAM-based FPGAs under the CERN mixed-field radiation environment," *IEEE Trans. Nucl. Sci.*, vol. 65, no. 8, pp. 1511–1518, Aug. 2018.

[29] M. Tali *et al.*, "Mechanisms of electron-induced single-event upsets in medical and experimental linacs," *IEEE Trans. Nucl. Sci.*, vol. 65, no. 8, pp. 1715–1723, Aug. 2018.